

Mitigation of Root Defect in Laser and Hybrid Laser-Arc Welding

A model is developed that predicts the range of processing conditions that produce defect-free, complete-joint-penetration welds

BY J. J. BLECHER, T. A. PALMER, AND T. DEBROY

ABSTRACT

Even though laser and hybrid laser-arc welding processes can produce single-pass, complete-joint-penetration welds in excess of 12 mm, root defects, such as root humping, have been observed at these greater plate thicknesses. The competition between the surface tension and the weight of the liquid metal in the weld pool is expected to govern root-defect formation. A series of laser and hybrid laser-gas metal arc welds has been completed in which each force is independently varied. The internal morphologies of the resulting root defects are characterized by X-ray computed tomography and found to vary significantly when welding with either the laser or hybrid laser-arc process. In order to compute the surface tension and liquid metal weight, a model based on the approximate geometry of the weld pool is developed and successfully predicts the range of processing conditions where root defects form. Process maps are then constructed for low-carbon steel and 304 stainless steel alloy systems. These maps can then be used to select welding parameters that produce defect-free complete-joint-penetration welds over a wide range of plate thicknesses.

KEYWORDS

• Laser Welding • Root Defect • Hybrid Welding • Carbon and Low-Alloy Steels

Introduction

High-power laser and hybrid laser-arc welding (Refs. 1–5) offer faster welding speeds, lower heat inputs, and deeper penetration over traditional arc welding processes in a range of different construction and fabrication industries (Ref. 6). However, these processes are also susceptible to unique defects associated with their high aspect ratio and deep penetration. Two of the most common of these defects include porosity from keyhole instability in partial-penetration welds (Refs. 7–9) and complete-joint-penetration welding root defects. The latter defect has also been called

chain of pearls (Ref. 10), dropping (Ref. 11), and root humping (Ref. 12). and is characterized by the formation of weld metal spheroids at the bottom surface of a complete-joint-penetration weld. An example of root defects in a DH36 steel hybrid laser-arc weld is shown in Fig. 1A. As higher laser powers become available and deeper penetrations are obtained, these defects will become more problematic, and a deeper understanding of the mechanisms driving these defects will be necessary to take advantage of these high laser powers.

Root defects have been characterized at both high (Refs. 13–16) and low (Refs. 11, 13, 17, 18) heat inputs.

Consequently, changes in laser power or welding speed resulted in the appearance or disappearance of root defects. For example, in 304 stainless steel, Zhang et al. (Ref. 14) and Kaplan and Wiklund (Ref. 16) found that root defects occur at lower welding speeds (i.e., higher heat input) during laser welding of 12- and 16-mm-thick plates, respectively. In other cases, increasing the heat input leads to acceptable welds. Havrilla et al. (Ref. 11) increased the laser power by 1 kW from 7.75 to 8.75 kW at a constant welding speed to eliminate root defects in 12-mm-thick steel. Ilar et al. (Ref. 12) employed high-speed imaging to study the formation of root defects in real time during the laser welding of 8-mm-thick 304 stainless steel plate. The high-speed videos showed the initiation of bulges immediately behind the keyhole, and these bulges would occasionally build up and solidify as root defects. Ilar et al. (Ref. 12) concluded that gravity, surface tension, and melt availability play a role in the formation of root defects.

One method for avoiding root defects is supporting the weld pool from the bottom through the use of electromagnetic forces from an oscillating magnetic field (Refs. 15, 19, 20). Bachmann et al. (Refs. 15, 20) complemented physical experiments by utilizing a 3D numerical heat transfer and fluid flow model to calculate the EM forces necessary to balance the hydrostatic pressure, which promoted root defects in 10- and 20-mm-thick steel and aluminum plates, respectively.

J. J. BLECHER (jjb5120@psu.edu) and T. DEBROY are with the Department of Materials Science and Engineering, and T. A. PALMER is with the Applied Research Laboratory, The Pennsylvania State University, University Park, Pa.

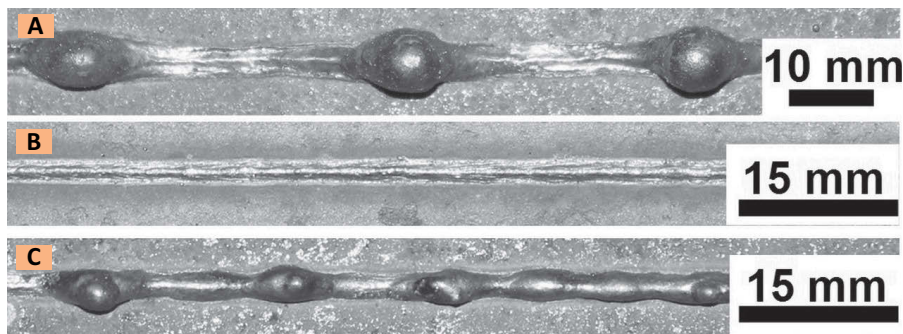
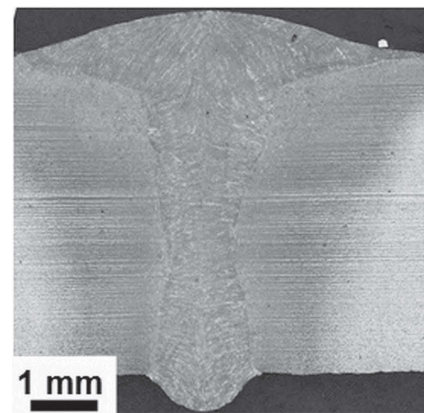
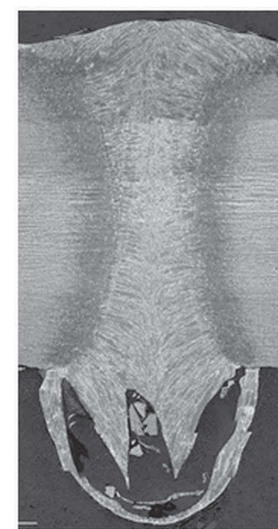


Fig. 1 — A — The typical weld root defects formed during hybrid laser-gas metal arc welding with a laser power, welding speed, and welding wire feed rate of 5 kW, 30 mm/s, and 229 mm/s, respectively; B — the roots of hybrid welds made under identical process conditions (welds 7, 8) without bottom surface oxide scale; C — with bottom oxide scale. On the plate with scale, root defects formed due to the low surface tension.



A



B

Fig. 2 — A — A comparison of the transverse hybrid weld (welds 7, 8) cross sections with identical welding conditions with the exception of bottom surface oxide scale, which was not present; B — the bottom surface oxide scale was present. The sizes of the welds are similar, suggesting that the weight of the liquid metal is similar and that the reduction in surface tension is due to the oxide scale presence, which led to the root defects.

However, the predicted EM force values were slightly less than the experimental values necessary to hold the liquid in place since only the weight of the liquid metal column above the bottom pool surface was taken into account. While EM support can be used to weld thick sections, utilizing the process in a production environment may not be practical, and the application of EM forces can change the fluid flow patterns during welding (Ref. 20). Therefore, it is necessary to develop a deeper understanding of the conditions that promote root defect formation in order to intelligently select welding parameters that suppress it.

In this paper, the formation of root defects is investigated for laser and hybrid laser-arc welding under a variety of welding conditions. For the first time, the 3D internal structure of the root defect nuggets in a structural steel plate weld was characterized by X-ray-computed tomography (CT) and was found to depend on the welding process employed. The melt volume and the surface tension of the molten DH36 steel were independently varied to determine

the effect of each on root defect formation. Melt volume was varied by changing the heat input of the welds, and surface tension was altered by removing the oxide scale on the bottom surface of the plate prior to welding. Increasing melt volume or decreasing surface tension led to root defects being formed. In order to quantify each effect, a force balance considering the weight of the liquid steel and the surface tension at the weld root is developed for an idealized weld pool and used to determine the conditions for the formation of root defects. Process maps for defect-free, complete-joint-penetration laser welds, for which substantial experimental results have been reported, and selected hybrid laser-arc welds were developed for low-carbon steel and 304 stainless steel.

Experimental Methods

Bead-on-plate laser and hybrid laser-arc welds were performed on 4.8- and 9.8-mm-thick DH36 steel plate. An IPG Photonics® YLR-12000-L ytterbium fiber laser with a Precitec® YW50 welding head was used for laser

Table 1 — Welding Conditions for LBW and HLAW Welds

Weld Number	Oxide Removed	Welding Process	Plate Thickness (mm)	Root Defects	Weld Speed (mm/s)	WFS (mm/s)
1	no	LBW	4.8	no	30	—
2	no	LBW	4.8	no	40	—
3	no	LBW	9.5	yes	15	—
4	no	HLAW	4.8	yes	30	127
5	no	HLAW	4.8	yes	30	152
6	no	HLAW	4.8	yes	30	229
7	yes	HLAW	4.8	no	40	127
8	no	HLAW	4.8	yes	40	127

Note: Oxide removed refers to the bottom surface oxide scale being removed.

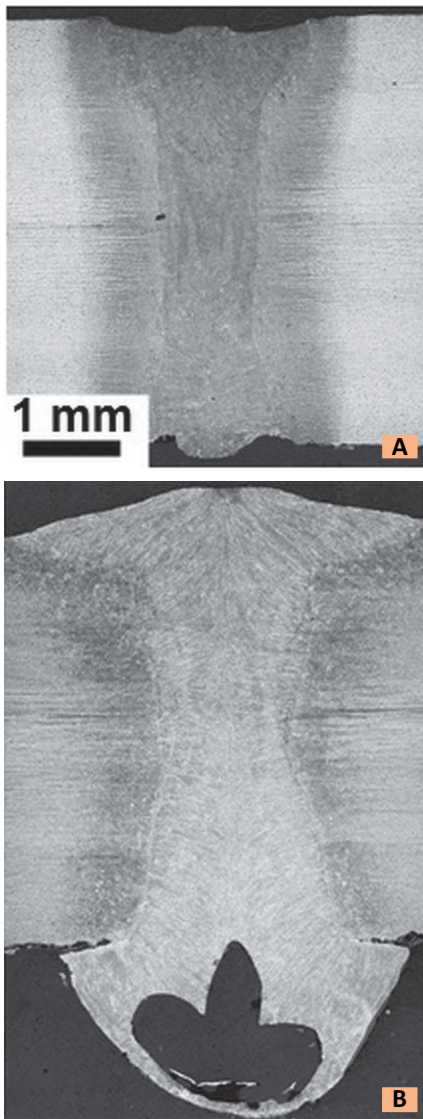


Fig. 3 — The transverse weld cross sections for: A — A laser weld (weld 1); B — a hybrid weld (weld 4) are shown. The laser conditions are the same, but the hybrid weld has increased heat input, larger amount of melted volume, and greater weight that must be supported by the surface tension force.

welding. The optics system utilizes collimating and focusing lenses with 200- and 500-mm focal lengths, respectively. The 1- μm laser wavelength is transported to the welding head through a 200- μm -diameter process fiber. The focused spot size and full divergence angle were measured with a Primes[®] Focus Monitor and are 0.52 mm and 64 mrad, respectively. A Lincoln Electric[®] Power Wave 455 M/STT power source with a Binzel[®] WH 455D water-cooled welding gun was used with ER

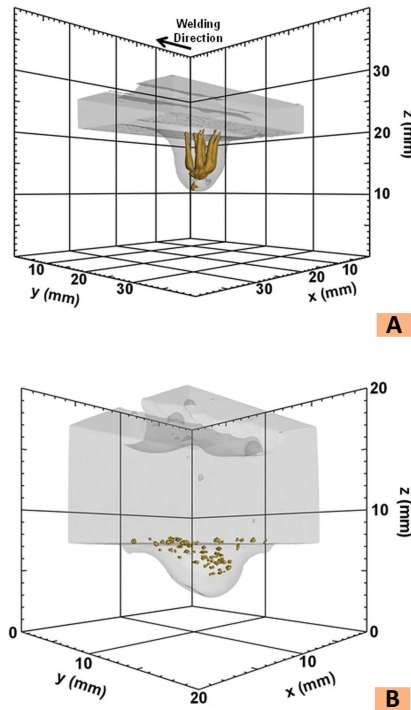


Fig. 4 — The internal structure of root defects in: A — Hybrid laser-gas metal arc weld in 4.8-mm-thick plate (weld 6). The direction of welding is indicated by the arrow. The strands of porosity that stretch from the bottom of the plate and connect in the center of the defect were common in all the hybrid welds where root defects formed; B — laser weld in 9.5-mm-thick plate (weld 3) as determined by X-ray computed tomography. Only individual pores are observed. Evidence of gouging due to material loss to root defects can be observed at the top of the plate.

70S-6 welding wire for the hybrid welding experiments.

In both the laser and hybrid laser-arc welding processes performed here, laser power, defocus, laser-arc separation distance, and arc voltage were kept constant at 5 kW, 8 mm, 3 mm, and 31 V, respectively, while wire feed speed, arc current and travel speed were varied when welding on 4.8-mm-thick plate. A positive 8-mm defocus indicates that the position of focus is above the plate. When welding on a 9.8-mm-thick plate, 7-kW laser power and zero defocus were selected. Additionally, to test the effect of the oxide presence on the bottom surface, two types of plate were used, one with only the top surface of the plate sand blasted to remove the oxide. The other

plate had the oxide removed on both sides. A summary of the welding parameters is given in Table 1. Oxide removed refers to whether the oxide scale was removed on both sides prior to welding. The welding processes were laser beam welding (LBW) and hybrid laser-arc welding (HLAW). Standard metallographic techniques were used to inspect the transverse cross-sections of the welds.

X-ray CT images were captured with a General Electric[®] v|tome|x CT system. The accelerating voltage and current for each scan were 280 kV and 180 μA , respectively. The voxel (i.e., 3D pixel) size with a magnification of 20 \times was 50 μm . DatosX[®] software handled the reconstruction of the individual X-ray images to produce the 3D image. The defect detection module in the Volume Graphics[®] VGStudio Max software was used to highlight the internal pore structure of the weld defects.

Results and Discussion

Root Defect Formation and Characterization

Based on previous research (Refs. 12, 15, 19, 20), surface tension and weld pool volume are thought to play a part in the formation of root defects. The surface tension at the bottom of the plate will restrain the liquid metal in the weld pool and discourage root defect formation. On the other hand, the weight of the molten metal in the weld pool will act to promote the formation of root defects. The competition between these two forces will determine whether defects will form.

In order to investigate the relationship between the surface tension and weld pool volume, both were independently varied during welding experiments. The presence of oxygen in molten iron has a significant effect on the surface tension. At high oxygen contents between 0.06 and 0.1 wt-%, the surface tension of liquid iron is lowered by 50% or more (Ref. 21) of its oxygen-free value, 1.91 N/m (Ref. 22). Oxygen content can be controlled indirectly by the removal of the oxide scale, which is present on both surfaces of the plate. In these experiments, welds with a high surface tension were ensured by first removing the oxide scale from both surfaces of

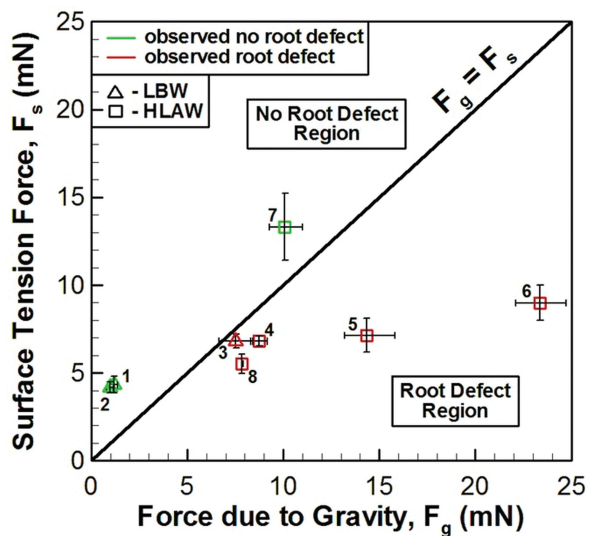


Fig. 5 — The comparison of surface tension force and weight force for the experimental welds considered. The numbers next to each weld indicate the processing conditions as shown in Table 1. Compared to experimental results, all the welds are found to be on the correct side of the $F_g = F_s$ line.

the steel plate. Low surface tension weld pools were acquired by only removing the oxide scale from the top surface and not grinding the bottom surface. Oxygen pickup is a contributor but not the sole source of root defects. In this case, the oxide scale acts as a source of oxygen that leads to a lower surface tension of the molten metal at the root of the weld but is not a necessary condition for root defect formation. The volume of the weld pool was varied by increasing the heat input by transitioning from laser to hybrid laser-arc welding or by increasing plate thickness. Higher heat inputs and greater plate thicknesses produce more molten metal during complete joint penetration welding.

In examining the effect of lower surface tension, hybrid welds (welds 7,

8) were made under the same conditions, with the exception of the oxide scale presence on the bottom surface. The weld without scale (weld 7) formed no root defects. A comparison of the bottom surfaces and transverse weld cross sections are shown in Fig. 1B, C and Fig. 2, respectively. In Fig. 1, irregularly spaced root defects can be observed in the weld with bottom surface oxide scale. While the weld without scale on the bottom surface, there are no observable defects. As can be observed in Fig. 2, root defects have a profound effect on the weld cross section. The weld without scale has a clearly identifiable arc zone at the top, which is much wider than the rest of the weld. In the weld with scale, the weld width is

much narrower, and the complex shape of the porosity in the root defect nugget is observable. Eleven hybrid welds were made with and eight hybrid welds made without bottom surface oxide scale. In all cases, the welds without bottom surface scale did not form root defects, while those with scale did form defects.

The effect of heat input and liquid metal volume on the root defect formation was investigated next for a series of welds made at a travel speed of 30 mm/s. As shown in Table 1, the laser weld (weld 1) has a heat input of 167 J/mm, while the hybrid welds (welds 4–6) had estimated heat inputs between 426 and 695 J/mm. The higher heat inputs should increase the size of the weld pool, which will increase the overall weight that must be balanced against the surface tension force at the bottom of the pool. At the lowest heat input, there were no root defects, but defects formed at the high heat inputs. The effect of heat input on the size of the weld and amount of material melted can be observed in

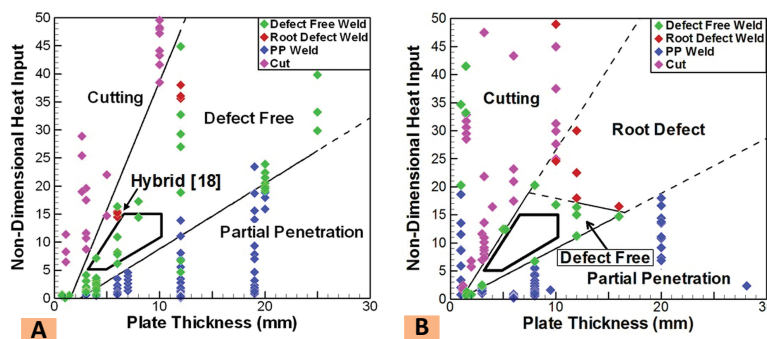


Fig. 6 — Process maps for: A — Low-carbon steels; B — 304 stainless steel — were constructed from available reports of laser welding and cutting experiments. The maps indicate with what processing conditions acceptable complete penetration welds can be made with respect to other interaction modes.

Fig. 3, which shows the transverse weld cross sections of the laser weld (weld 1) and the lowest heat input hybrid weld (weld 4). The hybrid weld is much larger in terms of cross-sectional area compared to the laser weld, and the high pool volume combined with the suppression of surface tension from the bottom surface scale promoted the formation of root defects.

Postweld observation showed that some of the defect nuggets were missing portions of the outer wall, which can be seen in one of the nuggets of Fig. 1C and indicates that porosity may be present. In Figs. 2 and 3, micrographs show complex pore shapes. The internal structure of the root defect nuggets was characterized with X-ray CT, which nondestructively evaluates internal defects by differentiating regions of different density. Within a metal structure, pores appear brighter since fewer X-rays are absorbed.

Typical internal structures of root defects formed during hybrid laser-arc welding and laser welding are shown in Fig. 4. The porosity is represented by the yellow colored shapes within the defects. The large pore in the hybrid weld is fully interconnected. Eight arms start at the edges of the weld and extend down to the bottom of the root defect nugget where they connect to a large central pore. This interconnected porosity contrasts with pores shown in Figure 4B for a laser weld fabricated in thicker plate. In this defect, there is only a dispersion of smaller spherical pores, which are only present in the top half of the defect. Large gouges in the top surface resulting from the loss of material to the defect are also visible in Fig. 4B.

Clearly, the laser and hybrid welding processes produced different pore shapes and sizes within the weld defects. Typically, in laser welding processes, where large spherical pores are present, keyhole collapse (Ref. 7) results in pores centered on the laser beam axis. Based on video evidence of root defects forming and growing along the length of the pool away from the keyhole (Ref. 12) and X-ray CT images of complex pore networks and different characteristics for different welding processes, keyhole dynamics probably cannot be used to explain the porosity structures within the weld defect nuggets. The most likely explana-

tion is that the additional forces in arc welding, such as the arc pressure and droplet impact force, led to the network of pores observed in Fig. 4A.

Mechanism of Root Defect Formation

The formation of weld root defects can be viewed as a force balance between the weight of the liquid metal in the weld pool and the surface tension force. A model has been developed to calculate the magnitude of each force and utilizes an approximate weld pool shape and measured weld bead dimensions. The details of the model are given in Appendix A. The results of the force balance between weight and surface tension are shown in Fig. 5. The numbers next to each point indicate which weld is plotted. Error bars represent the spread in values calculated with the uncertainty for each measured dimension given in Table 2. The model is physically consistent, since as heat input increases, the calculated values for weight due to gravity and surface tension force also increase. The $F_g = F_s$ line defines the boundary between regions where root defects will (to the right of the line) and will not (to the left of the line) occur.

The laser welds (welds 1–3) have the lowest weight forces (i.e., points farthest to the left in Fig. 5) due to the low heat input of the laser and the resulting small pool volumes compared to hybrid welds. Laser welds fabricated on 4.8-mm plate (welds 1, 2) did not form a defect since the surface tension force of 4 mN easily restrained the weight force of 1 mN. However, when complete joint penetration laser welds were made on thicker plate of 9.5 mm (weld 3), the weight force increased to 7.5 mN and exceeded the surface tension of less than 7 mN, and defects formed. The force balance captures the difference in plate thicknesses and predicts the observed outcome for the laser welds.

For the laser and hybrid laser-arc welds with the same 30 mm/s welding speed (welds 1, 4–6), the model predicts increasing weight due to gravity from 1 to 23 mN due to increasing heat input, but the surface tension only increased from 4 to 9 mN. The model predictions for these welds agree with the experimental observations. The force balance also captures the differences in welds on plates with and without bottom surface

oxide and identical process conditions (welds 7, 8) with similar weight forces of 8 and 10 mN, respectively. With the presence of the oxide scale, though, weld 8 possesses only 40% of the surface tension force of weld 7, which had no oxide scale. As a whole, agreement is good between the observed and predicted formation of root defects with all of the green symbols, indicating no observed root defects, falling above the $F_g = F_s$ line and all the red symbols, indicating observed defects, below the same line. These results indicate that representation of the root defect formation phenomenon as a quantitative force balance between weight and surface tension allows for a qualitative prediction of an important welding defect.

Process Maps for Complete Joint Penetration Laser Welding

The results described above indicate that both heat input and plate thickness affect the formation of root defects in DH36 steel and are expected to play a role in other alloys. For given laser welding parameters, material properties, and plate thicknesses, however, the developed model cannot provide a broader predictive capability of root defect formation. Additionally, the process parameters that produce defect-free complete-joint-penetration welds are bounded by other laser-material interaction modes, such as cutting and partial-penetration laser welding. In order to address these additional complexities, process maps that tie together laser welding parameters, material properties, heat input, plate thickness, and laser-material interaction modes are constructed for different alloy systems. Comparison of process maps for different alloys should show where similarities exist and what conclusions apply across material types.

Process maps have been constructed for laser processing of low-carbon steels and 304 stainless steel. The nondimensional heat input per unit length, which is similar to that used by De and DebRoy (Ref. 23) includes laser welding parameters and material properties and is defined as

$$H^* = \frac{\eta P}{\rho(h + \Delta H_v)\pi r_b^2} \quad (1)$$

Table 3 — Values Used to Construct the Process Maps

Alloy	$\eta - 1\mu\text{m}$	$\eta - 10.6\mu\text{m}$	ρ (kg/m ³)	h (kJ/kg)	ΔH_v (kJ/kg)
Steel	0.34	0.12	7030	2390	6260
304SS	0.34	0.12	7070	2290	6330

Note: Absorptivity, η , depends on the wavelength of the laser beam.

where η is absorptivity, P is laser power, r_b is the laser beam radius at focus, U is the welding speed, ρ is the liquid metal density, h is the enthalpy of the liquid at the boiling point, and ΔH_v is the heat of vaporization. Both the numerator and denominator have units of energy per unit length, J/m. Equation 1 compares the amount of energy absorbed from the laser per unit length in the numerator to the amount of energy per unit length necessary to heat the alloy from room temperature to the boiling point (denominator). For the experiments considered here, H^* is typically greater than one, indicating that absorbed laser energy is a multiple of the energy to heat the alloy to the boiling point. The material property values that were used to calculate H^* for each alloy are given in Table 3. Estimated resistivities (Ref. 24) were used to calculate absorptivity (Ref. 25), and density, enthalpy, and heat of vaporization were obtained from available references (Refs. 24, 26).

When H^* is plotted as a function of plate thickness, four regions defining cutting, complete-joint-penetration weld without defects, complete-joint-penetration weld with defects, and partial-penetration weld, can be identified. In the case of cutting low-carbon steel or stainless steel in the presence of oxygen gas, laser energy accounts for approximately half of the total energy input into the system with oxidation of liquid iron accounting for the other half (Refs. 27, 28). Other processes, such as hybrid laser-arc welding, are not considered in these maps, but as shown previously, the addition of another heat source can increase the chances of root defect formation.

The process maps for the laser welding of low-carbon steel (Refs. 18, 27, 29–53) and 304 stainless steel (Refs. 14–16, 39, 40, 54–70) are shown in Fig. 6. Experimental H^* data for cutting, complete-joint-penetra-

tion welds without root defects, and partial penetration welds are determined by macrographs of the welds or explicit statements in the text and plotted for every material type. Root defects reported in the literature are assumed to form because of the competition between the surface tension and liquid metal weight forces and not other phenomena, such as keyhole instability, which leads to macroporosity. The lines defining each region are fit to the complete-joint-penetration laser welding data. All the conditions shown are for a laser only, except as indicated in Fig. 6A, where a set of hybrid laser-GMAW conditions (Ref. 18) is used to show another case of root defects in low-carbon steel.

The points indicating root defect formation for low-carbon steel in 12-mm-thick plate (Ref. 31) are situated close to the cutting-complete joint penetration transition line. On the other hand, because of the availability of data, a line indicating the transition from defect-free welds to welds with root defects can be drawn for 304 stainless steel and fully encloses the complete-joint-penetration laser welding space for the alloy. According to the process map, the laser welding parameters for complete-joint-penetration welds in excess of 16 mm are very limited, so only careful selection of processing parameters can produce a defect-free weld. For the same space in low-carbon steel, relatively thick plates of 25 mm can be welded at nondimensional heat inputs of less than 40.

Comparison of the process maps shows relatively similar behaviors at lower heat inputs and plate thicknesses. This similarity across process maps is highlighted by the thick solid black line, which encloses an identical process space in the defect-free zone, and can be used to produce defect-free complete-joint-penetration welds for each alloy. For example, process parameters yielding an H^* of 12 will pro-

duce a defect-free weld in 8-mm-thick plate of low-carbon steel and 304 stainless steel. Identical H^* values for plate thicknesses between 3.5 and 10 mm can be used across alloy systems. The parameters shown in Fig. 6 can speed process parameter development, especially in thick plates, where greater heat inputs lead to longer cooling times between trial welds. For example, if laser optics are fixed (i.e., minimum laser beam radius cannot change), then welding engineers can quickly select nondimensional heat input from Fig. 6 for a given plate thickness and calculate via Eq. 1 the laser powers and welding speeds that will produce defect-free, complete-joint-penetration welds.

At higher heat inputs and plate thicknesses, the behaviors of each alloy diverge. A very small defect-free complete-joint-penetration process space is observed in 304 stainless steel. The opposite is observed in low-carbon steels. The process maps indicate that two conditions are necessary before root defects can form during laser welding. First, the plate thickness must be 10 mm or greater. Second, the nondimensional heat input must be greater than 16, which is also a minimum value associated with root defects. Once these two conditions are met, the formation of root defects becomes possible. However, as shown in the process maps, satisfying the conditions does not guarantee root defect formation. For example, the mean average H^* value for root defect formation in low-carbon steel and 304 stainless steel laser welds is 33, so the chances of forming root defects increases as the heat input increases.

From the process maps, 304 stainless steel is more susceptible to root defect formation than low-carbon steel. The reason is the difference in surface tension, which is 1.91 N/m (Ref. 22) and 1.17 N/m (Ref. 79) for steel and stainless steel, respectively. The density of each liquid alloy is 7030 kg/m³ for

steel and 7070 kg/m³ for 304 stainless steel (Ref. 24). Both surface tension and density should affect the formation of root defects as shown in Eq. A5 and A7, and only surface tension is very different between the two alloys.

Close inspection of Fig. 6A, B indicates that root defects are associated with relatively higher heat inputs. For low-carbon steel, the root defects in both laser and hybrid welding conditions are close to the cutting transition line, indicating high heat input. In the case of 304 stainless steel, all the heat inputs associated with root defects are greater than the defect-free heat inputs for the same plate thicknesses, 10, 12, and 16 mm.

Some researchers have concluded that the root defects are associated with low heat input (Refs. 11, 18, 31). However, the data compiled in Fig. 6A, B suggest that the opposite is true. In cases where lower heat inputs certainly led to root defect formation, it appears that the researchers were already operating at a high heat input. For example, for 12-mm-thick low-carbon steel plate (Ref. 31) and nondimensional heat inputs between 35 and 40, defects formed, but at lower heat inputs of 29 and 33 and higher heat inputs of 45 and 50 root defects did not form. Additionally, all of these heat inputs are relatively high because complete-joint-penetration defect-free welds were made at nondimensional heat inputs as low as 5 and 7 (Ref. 31). By considering the whole range of process parameters captured in the nondimensional heat input parameter, the fact that root defects are a high heat input phenomenon becomes clear and unambiguous.

Summary and Conclusions

The root defect in complete-joint-penetration laser and hybrid laser-arc welding has been experimentally and theoretically investigated. Welding parameters, plate preparation, and plate size were varied to produce welds with and without root defects. Optical microscopy and X-ray CT characterized the internal structure of the defect nuggets for different welding processes. A force balance between the weight of the liquid metal and the surface tension was developed to describe the competing forces driving the onset of

defect formation. Process maps for two alloy systems have been constructed based on the experimental welding and cutting parameters reported in the literature. The conclusions of this work are listed below.

1) The qualitative effect of surface tension and weight of liquid metal on the formation of root defects was determined by varying the welding parameters. A decrease in surface tension due to the presence of oxide scale on the bottom plate surface led to the defect formation while no defects formed for the same conditions on a plate with the oxide scale removed. Larger weld pools were formed either by increasing heat input with the addition of an arc or laser welding on 9.5-mm-thick plate. The larger pools led to root defects, while the laser welds on 4.8-mm-thick plate formed smaller pools and did not result in root defects.

2) With the use of X-ray CT, the internal structure of defect nuggets formed during hybrid laser-arc and laser welding were found to be different. In hybrid welding, the structure consisted of a network of large pore strands that stretched from the edge of the bottom weld bead to the center of the defect nugget. On the other hand, defect nuggets resulting from a laser weld showed a dispersion of small spherical pores. The additional arc pressure and droplet impact forces in hybrid welding are the likely factors for the difference in porosity structure.

3) Based on the observations of surface tension and weight of liquid metal, a force balance between the two was developed for an idealized weld pool and applied to the experimental conditions used in the study. The force balance calculations matched the experimental observations in terms of root defect formation for all of the cases considered. The results showed that the force balance has utility for predicting the defect formation, assuming the pool geometry is known or can be calculated.

4) The process maps for low-carbon steel and 304 stainless steel revealed that identical H* values between 5 and 15 can be used to fabricate defect-free welds in plate thicknesses between 3.5 and 10 mm for the two alloys considered.

5) The compiled data show that two conditions, plate thicknesses greater

than 10 mm and H* values greater than 15, must be met before root defects can form. Consideration of the heat inputs necessary to form root defects in low-carbon steel and stainless steel demonstrated that root defects are a high heat input phenomenon, so in most cases, reducing heat input will eliminate defect formation.

Acknowledgments

The authors would like to thank Mr. Jay Tressler for performing the welding experiments and Mr. Ed Good for preparing the metallographic and X-ray specimens. This research was performed using funding received from the DOE Office of Nuclear Energy's Nuclear Energy University Programs under Grant Number 120327.

References

1. Zhang, J., Shan, J. G., Ren, J. L., and Wen, P. 2013. Reducing the porosity in die-cast magnesium alloys during laser welding. *Welding Journal* 92(4): 101-s to 109-s.
2. Roepke, C., Liu, S., Kelly, S., and Martukanitz, R. 2010. Hybrid laser arc welding process evaluation on DH36 and EH36 steel. *Welding Journal* 89(7): 140-s to 150-s.
3. Sachedz-Amaya, J. M., Boukha, Z., Amaya-Vazquez, M. R., and Botana, F. J. 2012. Weldability of aluminum alloys with high-power diode laser. *Welding Journal* 91(5): 155-s to 161-s.
4. Victor, B., Farson, D. F., Ream, S., and Walters, C. T. 2011. Custom beam shaping for high-power fiber laser welding. *Welding Journal* 90(6): 113-s to 120-s.
5. Wu, S. C., Yu, X., Zuo, R. Z., Zhang, W. H., Xie, H. L., and Jiang, J. Z. 2013. Porosity, element loss, and strength model on softening behavior of hybrid laser arc welded Al-Zn-Mg-Cu alloy with synchrotron radiation analysis. *Welding Journal* 92(3): 64-s to 71-s.
6. Ribic, B., Palmer, T. A., and DebRoy, T. 2009. Problems and issues in laser-arc hybrid welding. *Int. Mater. Rev.* 54(4): 223-244.
7. Matsunawa, A., Kim, J.-D., Seto, N., Mizutani, M., and Katayama, S. 1998. Dynamics of keyhole and molten pool in laser welding. *J. Laser Appl.* 10(6): 247-254.
8. Tucker, J. D., Nolan, T. K., Martin, A. J., and Young, G. A. 2012. Effect of travel speed and beam focus on porosity in alloy 690 laser welds. *JOM* 64(12): 1409-1417.

9. Madison, J. D., and Aagesen, L. K. 2012. Quantitative characterization of porosity in laser welds of stainless steel. *Scripta Mater.* 67(9): 783–786.
10. Salminen, A., Piili, H., and Purtonen, T. 2010. The characteristics of high power fibre laser welding. *Proc. IMechE, Part C J. Mech. Eng. Sci.* 224(C5): 1019–1029.
11. Havrilla, D., Rominger, V., Holzer, M., Harrer, T., and Andreev, A. 2013. Advanced welding techniques with optimized accessories for high brightness 1 μm lasers. *Proc. SPIE 8603, High-Power Laser Mater. Process.: Lasers, Beam Deliv., Diagn., and Appl. II.* Ed. F. Dorsch, 8603ON. SPIE.
12. Ilar, T., Eriksson, I., Powell, J., and Kaplan, A. 2012. Root humping in laser welding — an investigation based on high speed imaging. *7th Conf. Laser Assist. Net Shape Eng./Int. Conf. Photonic Eng.* Eds. M. Schmidt, F. Vollertsen, and M. Geiger, pp. 27–32. Elsevier Sci.
13. Punkari, A., Weckman, D. C., and Kerr, H. W. 2003. Effects of magnesium content on dual beam Nd:YAG laser welding of Al-Mg alloys. *Sci. Technol. Weld. Joining* 8(4): 269–281.
14. Zhang, M., Chen, G., Zhou, Y., and Liao, S. 2014. Optimization of deep penetration laser welding of thick stainless steel with a 10 kW fiber laser. *Mater. Des.* 53: 568–576.
15. Bachmann, M., Avilov, V., Gumenyuk, A., and Rethmeier, M. 2014. Experimental and numerical investigation of an electromagnetic weld pool support system for high power laser beam welding of austenitic stainless steel. *J. Mater. Process. Technol.* 214(3): 578–591.
16. Kaplan, A. F. H., and Wiklund, G. 2011. Advanced welding analysis methods applied to heavy section welding with a 15 kW fibre laser. *Weld. World* 53: 295–300.
17. Ohnishi, T., Kawahito, Y., Mizutani, M., and Katayama, S. 2013. Butt welding of thick, high strength steel plate with a high power laser and hot wire to improve tolerance to gap variance and control weld metal oxygen content. *Sci. Technol. Weld. Joining* 18(4): 314–322.
18. Piili, H., Salminen, A., Harkko, P., and Lehtinen, J. 2008. Study of phenomenon of fibre-laser-mig/mag-hybrid-welding. *ICALEO 2008 – 27th Int. Congr. Appl. Lasers Electro-Opt.* pp. 506–515. Laser Inst. of America.
19. Avilov, V. V., Gumenyuk, A., Lammers, M., and Rethmeier, M. 2012. PA position full penetration high power laser beam welding of up to 30-mm-thick AlMg₃ plates using electromagnetic weld pool support. *Sci. Technol. Weld. Joining* 17(2): 128–133.
20. Bachmann, M., Avilov, V., Gumenyuk, A., and Rethmeier, M. 2012. Numerical simulation of full penetration laser beam welding of thick aluminium plates with inductive support. *J. Phys. D: Appl. Phys.* 45(3): 035201.
21. Keene, B. J. 1988. Review of data for the surface tension of iron and its binary alloys. *Int. Mater. Rev.* 33(1): 1–37.
22. Keene, B. J. 1993. Review of data for the surface tension of pure metals. *Int. Mater. Rev.* 38(4): 157–192.
23. De, A., and DebRoy, T. 2004. A smart model to estimate effective thermal conductivity and viscosity in the weld pool. *J. Appl. Phys.* 95(9): 5230–5240.
24. Gale, W. F. 2004. *Smithells Metals Reference Book*, 8th Edition. Burlington, Mass., Elsevier Butterworth-Heinemann.
25. Dowden, J., and Phiroze, K. 1995. A mathematical investigation of the penetration depth in the keyhole welding with continuous CO₂ lasers. *J. Phys. D: Appl. Phys.* 28(11): 2252–2261.
26. Pakratz, L. B. 1982. Thermodynamic properties of elements and oxides. U.S. Dept. of the Interior, Bureau of Mines, District of Columbia.
27. Hsu M. J., and Molian, P. A. 1994. Thermochemical modeling in CO₂ laser cutting of carbon steel. *J. Mater. Sci.* 29(21): 5607–5611.
28. Ivarson, A., Powell, J., and Magnusson, C. 1991. The role of oxidation in laser cutting stainless and mild steel. *J. Laser Appl.* 3(3): 41–45.
29. Krasnoperov, M. Y., Pieters, R. R. G. M., and Richardson, I. M. 2004. Weld pool geometry during keyhole laser welding of thin steel sheets. *Sci. Technol. Weld. Joining* 9(6): 501–506.
30. Sokolov, M., Salminen, A., Kuznetsov, M., and Tsubulskiy, I. 2011. Laser welding and weld hardness analysis of thick section S355 structural steel. *Mater. Des.* 32(10): 5127–5131.
31. Rominger, V., Haug, P., Speker, N., and Holzer, M. 2013. High-power full penetration welding behavior. *Laser Tech. J.* 10(3): 36–40.
32. Assuncao, E., Ganguly, S., Yapp, D., Williams, S., and Paradowska, A. 2011. Characterization of residual stress state in laser welded low carbon mild steel plates produced in keyhole and conduction mode. *Sci. Technol. Weld. Joining* 16(3): 239–243.
33. Cui, C., Hu, J., Gao, K., Pang, S., Yang, Y., Wang, H., and Guo, Z. 2008. Effects of process parameters on weld metal keyhole characteristics with CO₂ laser butt welding. *Lasers Eng.* 18(5–6): 319–327.
34. Hamatani, H., Miyazaki, Y., Otani, T., and Ohkita, S. 2006. Minimization of heat-affected zone size in welded ultra-fine grained steel under cooling by liquid nitrogen during laser welding. *Mater. Sci. Eng. A* 426(1–2): 21–30.
35. Ion, J. C., Salminen, A. S., and Sun, Z. 1996. Process diagrams for laser beam welding of carbon manganese steels. *Welding Journal* 75(7): 225-s to 232-s.
36. Oefele, F., Musiol, J., Zaeh, M. F. 2008. Influence of remote-laser-welding parameters for an 8 kW fibre laser on the seam quality of steels. *ICALEO 2008 – 27th Int. Congr. Appl. Lasers Electro-Opt.* pp. 399–405. Laser Inst. of America.
37. Mori, K., and Miyamoto, I. 1997. In-process monitoring of laser welding by the analysis of ripples in the plasma emission. *J. Laser Appl.* 9(3): 155–159.
38. Vollertsen, F., Grunenwald, S., Rethmeier, M., Gumenyuk, A., Reisgen, U., Olschok, S. 2010. Welding thick steel plates with fibre lasers and GMAW. *Weld. World* 54(3–4): R62–R70.
39. Brown, R. T. 2008. Keyhole welding studies with a moderate-power, high-brightness fiber laser. *J. Laser Appl.* 20(4): 201–208.
40. Nakamura, S., Sakurai, M., Kamimuki, K., Inoue, T., and Ito, Y. 2000. Detection technique for transition between deep penetration mode and shallow penetration mode and shallow penetration mode in CO₂ laser welding of metals. *J. Phys. D: Appl. Phys.* 33(22): 2941–2948.
41. Kumar, N., Kataria, S., Shanmugarajan, B., Dash, S., Tyagi, A. K., Padmanabham, G., and Raj, B. 2010. Contact mechanical studies on continuous wave CO₂ laser beam weld of mild steel with ambient and under water medium. *Mater. Des.* 31(8): 3610–3617.
42. Miranda, R., Quintino, L., Williams, S., and Yapp, D. 2010. Welding with high power fiber laser API5L-X100 pipeline steel. *5th Int. Mater. Symp./14th Conf. Soc.-Port.-Mater.* Eds. L. G. Rosa and F. Margarido, pp. 592–596. Trans Tech Publ.
43. Quintino, L., Costa, A., Miranda, R., Yapp, D., Kumar, V., and Kong, C. J. 2007. Welding with high power fiber lasers — a preliminary study. *Mater. Des.* 28(4): 1231–1237.
44. Suder, W. J., and Williams, S. 2014. Power factor model for selection of welding parameters in CW laser welding. *Opt. Laser Technol.* 56: 223–229.
45. Chen, S.-L. 1998. The effect of gas composition on the CO₂ laser cutting of mild steel. *J. Mater. Process. Technol.* 73(1–3): 147–159.
46. Lo, K. H. 2012. A comparative study on Nd:YAG laser cutting of steel and stainless steel using continuous, square, and sine waveforms. *J. Mater. Eng. Perform.* 21(6): 907–914.
47. Malikov, A. G., Orishich, A. M., and Shulyat'ev, V. B. 2009. Experimental optimization of the gas-assisted laser cutting of thick steel sheets. *Quantum Electron.* 39(6): 547–551.
48. O'Neill, W., and Steen, W. M. 1995. A three-dimensional analysis of gas entrainment operating during the laser-cutting process. *J. Phys. D: Appl. Phys.* 28(12):

- 12–18.
49. Powell, J., Al-Mashikhi, S. O., Kaplan, A. F. H., and Voisey, K. T. 2011. Fibre laser cutting of thin section mild steel: an explanation of the 'striation free effect'. *Opt. Lasers Eng.* 49(8): 1069–1075.
50. Shariff, S. M., Sundararajan, G., and Joshi, S. V. 1999. Parametric influence on cut quality attributes and generation of processing maps for laser cutting. *J. Laser Appl.* 11(2): 54–63.
51. Sobih, M., Crouse, P. L., and Li, L. 2007. Elimination of striation in laser cutting of mild steel. *J. Phys. D: Appl. Phys.* 40(22): 6908–6916.
52. Wandera, C., Kujanpaa, V., and Salmiinen, A. 2010. Laser power requirement for cutting thick-section steel and effects of processing parameters on mild steel cut quality. *Proc. IMechE Part B: J. Eng. Manuf.* 225(B5): 651–661.
53. Zaied, M., Miraoui, I., Boujelbene, M., and Bayraktar, E. 2013. Analysis of heat affected zone obtained by CO₂ laser cutting of low carbon steel (S235). *3rd Int. Congr. Adv. Appl. Phys. Mater. Sci.* Eds. A. Y. Oral, Z. B. Bahsi, and A. Sonmez, pp. 323–326. Amer. Inst. Phys.
54. Nath, A. K., Sridhar, R., Ganesh, P., and Kaul, R. 2002. Laser power coupling efficiency in conduction and keyhole welding of austenitic stainless steel. *Sadhana* 27: 383–292.
55. Bhargava, P., Paul, C. P., Mundra, G., Premsingh, C. H., Mishra, S. K., Nagpure, D., Kumar, A., and Kukreja, L. M. 2014. Study on weld bead surface profile and angular distortion in 6-mm-thick butt weld joints on SS304 using fiber laser. *Opt. Laser Eng.* 53: 152–157.
56. Nakabayashi, T., Wani, F., Hayakawa, A., Suzuki, S., and Yasuda, K. 2003. Thick plate welding with Nd:YAG laser and COIL. *1st Int. Symp. High-Power Laser Macroprocess.* Eds. I. Miyamoto, K. F. Kobayashi, K. Sugioka, R. Poprawe, H. Helvajian, pp. 416–421. SPIE.
57. Panstar, H., Salmiinen, A., Jansson, A., and Kujanpaa, V. 2004. Quality and costs analysis of laser welded all steel sandwich panels. *J. Laser Appl.* 16(2): 66–72.
58. Kawahito, Y., Mizutani, M., and Katayama, S. 2007. Elucidation of high-power fibre laser welding phenomena of stainless steel and effect of factors on weld geometry. *J. Phys. D: Appl. Phys.* 40(19): 5854–5859.
59. Ghany, K. A., and Newishy, M. 2005. Cutting of 1.2-mm-thick austenitic stainless steel sheet using pulsed and CW Nd:YAG laser. *J. Mater. Process. Technol.* 168(3): 438–447.
60. Hsu, M. J., and Molian, P. A. 1995. Off-axial, gas-jet-assisted, laser cutting of 6.35-mm-thick stainless steel. *Trans. ASME* 117(2): 272–276.
61. Ilavarasan, P. M., and Molian, P. A. 1995. Laser cutting of thick sectioned steels using gas flow impingement on the erosion front. *J. Laser Appl.* 7(4): 199–209.
62. Purtonen, T., and Salminen, A. 2014. A study on the effect of cutting position on performance of fiber laser cutting of stainless steel tubes. *Weld. World* 58(2): 193–204.
63. Sheng, P. S., and Joshi, V. S. 1995. Analysis of heat-affected zone formation for laser cutting of stainless steel. *J. Mater. Process. Technol.* 53(3–4): 879–892.
64. Sparkes, M., Gross, M., Celotto, S., Zhang, T., and O'Neill, W. 2008. Practical and theoretical investigations into inert gas cutting of 304 stainless steel using a high brightness fiber laser. *J. Laser Appl.* 20(1): 59–67.
65. Stelzer, S., Mahrle, A., Wetzig, A., and Beyer, E. 2013. Experimental investigations on fusion cutting stainless steel with fiber and CO₂ laser beams. *7th Int. WLT Conf. Lasers Manuf.* Eds. C. Emmelmann, M. F. Zaeh, T. Graf, and M. Schmidt, pp. 392–397. Elsevier Sci. BV.
66. Wandera, C., Salminen, A., and Kujanpaa, V. 2009. Inert gas cutting of thick-section stainless steel and medium-section aluminum using a high power fiber laser. *J. Laser Appl.* 21(3): 154–161.
67. Kuo, T. Y., and Jeng, S. L. 2005. Porosity reduction in Nd-YAG laser welding of stainless steel and inconel alloy by using a pulsed wave. *J. Phys. D: Appl. Phys.* 38(5): 722–728.
68. Rizzi, D., Sibillano, T., Calabrese, P. P., Ancona, A., and Lugara, P. M. 2011. Spectroscopic, energetic, and metallographic investigations of the laser lap welding of AISI 304 using the response surface methodology. *Opt. Lasers Eng.* 49(7): 892–898.
69. Hartwig, L., Ebert, R., Kloetzer, S., Weinhold, S., Dreschel, J., Peuckert, F., Schille, J., and Exner, H. 2010. Material processing with a 3 kW single mode fibre laser. *J. Laser Micro/Nanoeng.* 5(2): 128–133.
70. Kawahito, Y., Mizutani, M., Katayama, S. 2009. High quality welding of stainless steel with 10 kW high power fibre laser. *Sci. Technol. Weld. Joining* 14(4): 288–294.
71. Mills, K. C. 2002. *Recommended Values of Thermophysical Properties for Selected Commercial Alloys.* Cambridge, Woodhead.
72. Blecher, J. J., Palmer, T. A., and DebRoy, T. 2014. Solidification map of a nickel base alloy. *Metall. Mater. Trans. A* 45A(4): 2142–2151.
73. Brohnstein, I. N. 2007. *Handbook of Mathematics*, 5th Edition. New York, N.Y., Springer.
74. Halliday, D., Resnick, R., and Walker, J. 2005. *Fundamentals of Physics*, 7th Ed. Hoboken, N.J., John Wiley & Sons, Inc.
75. Lin, L., and Eagar, T. W. 1986. Presures produced by gas tungsten arcs. *Metall. Trans. B.* 17B(3): 601–607.
76. Rai, R., and DebRoy, I. 2008. Numerical simulation of heat transfer and fluid flow in GTA/ laser hybrid welding. *Sci. Technol. Weld. Joining* 13(8): 683–693.
77. Zhang, W., Kim, C.-H., and DebRoy, T. 2004. Heat and fluid flow in complex joints during gas metal arc welding — Part II: Application to fillet welding of mild steel. *J. Appl. Phys.* 95(9): 5220–5229.
78. Basu, S., and DebRoy, T. 1992. Liquid metal expulsion during laser irradiation. *J. Appl. Phys.* 72(8): 3317–3322.
79. He, X., Norris, J. T., Fuerschbach, P. W., and DebRoy, T. 2006. Liquid metal expulsion during laser spot welding of 304 stainless steel. *J. Phys. D: Appl. Phys.* 39(3): 525–534.
80. Garandet, J. P., Vinet, B., and Gros, P. 1994. Considerations on the pendant drop method: a new look at Tate's law and Harkin's correction factor. *J. Colloid Interface Sci.* 165(2): 351–354.

Appendix A

Calculation of Surface Tension and Liquid Metal Weight

To calculate the force balance between surface tension and liquid metal weight, the approximated weld pool is split into two general parts as illustrated in Fig. A1. The leading segment of the weld pool, where the laser is interacting with the liquid metal, is rounded and semicircular in shape and extends through the thickness of the plate. The trailing section of the weld, especially at higher welding speeds, can take a triangular appearance at the top surface but does not extend through the entire plate thickness. There is some boundary between the pool and solidified material that extends from the end of the pool on the top surface to the edge of the pool on the bottom surface. Similarly, the volume of the idealized weld pool, shown in Fig. A1, is split into two parts, a cylinder surrounded by half of a truncated cone, which are numbered 1 and 2, respectively, near the heat sources and an overlapping trapezoid base pyramid, which is divided between a rectangular base pyramid (3) and two triangle base pyramids (4 and 5). This idealized volume is comparable to numerical modeling results of partial-penetration laser welds made under similar conditions with depths of penetration close to the plate thickness

used here (Ref. 72).

The various shapes are numbered as 1) cylinder, 2) truncated cone, 3) rectangle base pyramid, and 4) and 5) triangle base pyramid. The volumes are calculated as (Ref. 73)

$$V_1 = \frac{1}{2}\pi d^2 t \quad (A1)$$

$$V_2 = \frac{1}{24}(\pi t)(D^2 + d^2 + Dd) - \frac{1}{2}V_1 \quad (A2)$$

$$V_3 = \frac{1}{2}d t l - \frac{1}{2}V_1 \quad (A3)$$

$$V_4 = V_5 = \frac{1}{2}(D - d)t l \quad (A4)$$

where d is the bottom surface weld width, t is the plate thickness, D is the top surface weld width, and l is the distance from the position of maximum weld width to the trailing edge of the weld pool. Plate thickness is known, and the top and bottom surface widths can be measured from the weld bead. The distance, l , can be estimated from the top surface weld bead. Three measurements were made for the values D , d , and l in each weld and are given in Table 2 along with the standard deviations.

Most of the liquid steel in the weld is supported partially by underlying solid material, which either solidified or never melted. So, the entire weight of the liquid metal is not supported by the surface tension force at the bottom of the pool. This situation is accounted for by assuming each column of liquid is supported by a surface acting as an inclined plane (Ref. 74). The volume of liquid unsupported by any surface is the cylinder lying in the center of the truncated cone. The force of the liquid metal in the idealized weld pool that must be supported by the surface tension force is

$$F_g = \rho g [V_1 + (V_2 + V_4 + V_5 + V_s) \sin^2 \theta_1 + V_3 \sin^2 \theta_2] \quad (A5)$$

where ρ is the density of liquid iron, 7200 kg/m^3 (Ref. 24), g is acceleration due to gravity, θ_1 is the angle that the cone and the triangle base pyramids make with the bottom of the plate, and θ_2 is the angle that the rectangle

base pyramid makes with the plate bottom. V_s is a small volume that is not considered in the five volumes and is determined by disc integration of triangle ABC in Fig. 7B.

Some of the welds considered are hybrid laser-arc welds, where filler metal is added to the molten pool. In this case, the filler metal was assumed to be spread evenly over the area of the idealized weld with each of the five volumes increasing based on top surface area fractions of each shape. The volume of filler metal added over the length of the weld pool is

$$V_M = \frac{V_w \pi d_w^2}{4} \frac{\frac{1}{2}D + l}{U} \quad (A6)$$

where v_w is the wire feed speed, d_w is the diameter of the filler metal wire, and U is the welding speed. The first fraction describes the volume of filler metal added to the weld per unit time. The time necessary for the arc to traverse the length of the weld pool is calculated in the second fraction. Additionally, arc pressure from the plasma will act on the weld pool during hybrid laser-gas metal arc welding. The total arc force has been measured by Lin and Eagar (Ref. 75) in gas tungsten arc welds for various torch angles and welding currents. The estimated forces (Ref. 75) are listed in Table 2, and since the arc is located over the rectangle base pyramid, the forces have been added to the rectangle base pyramid.

In the above derivations, recoil force and droplet impact force have not been taken into account. The recoil force results from evaporation at the molten pool surface, and the droplet impact force is due to the addition of liquid metal to the pool from the consumable electrode. The recoil pressure is a function of the equilibrium vapor pressure, which itself depends on the temperature of the liquid metal. Using the vapor pressure of liquid iron (Ref. 24), the recoil force (Ref. 76) with a 46 mm^2 weld pool surface area and 2500 K surface temperature is 0.4 mN . Due to the relatively low value of recoil force at a fairly high temperature, the effects of recoil pressure were neglected. Similarly, when

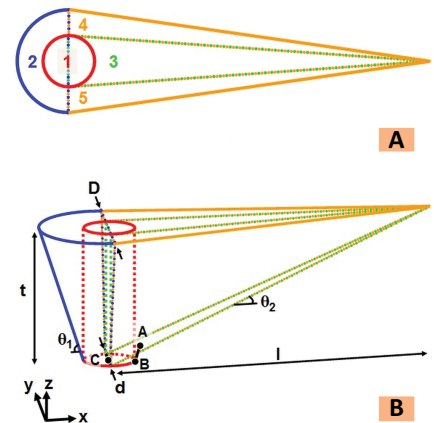


Fig. A1 — The idealized weld pool, which is used to estimate the volume and weight of the liquid metal, is shown as — A — A top-down view outlining the five volumes used to calculate total volume; B — a 3D view with the various variables, dimensions, and individual volumes.

the droplet mass and acceleration are estimated (Ref. 77) for the welding conditions studied, the maximum force is less than 1 mN , which is negligible compared to the other forces.

The surface tension force is the restraining force that holds the liquid metal in the pool and prevents the formation of the root defect. This force is calculated as (Refs. 78,79)

$$F_s = \pi \sigma d \quad (A7)$$

where σ is the surface tension of liquid steel at the melting point. In this geometry, the root of the weld pool acts as a pendant drop prior to detachment (Ref. 80). According to this formulation, the maximum surface tension force is normal to the plate. The determination of the surface tension for the pendant drop is calculated the same as Eq. A7 when the force is set equal to the weight of the droplet. For the plate that was ground on the bottom, the surface tension was taken as 1.91 N/m (Ref. 22), the value for pure iron. For those welds made on plates containing oxide scale on the bottom surface, the surface tension was taken as 0.88 N/m (Ref. 21), a value consistent with oxygen impurities in iron.